

See discussions, stats, and author profiles for this publication at: <https://www.researchgate.net/publication/6812060>

# Molecular Thermodynamics for Micellar Branching in Solutions of Ionic Surfactants

ARTICLE *in* LANGMUIR · OCTOBER 2006

Impact Factor: 4.46 · DOI: 10.1021/la061087q · Source: PubMed

---

CITATIONS

22

---

READS

20

2 AUTHORS, INCLUDING:



Vasily A. Andreev

American Institute of Chemical Engineers

9 PUBLICATIONS 44 CITATIONS

SEE PROFILE

# Articles

## Molecular Thermodynamics for Micellar Branching in Solutions of Ionic Surfactants

Vasily A. Andreev and Alexey I. Victorov\*

Department of Chemistry, St. Petersburg State University, Universitetsky prospect 26,  
198504, St. Petersburg, Russia

Received April 21, 2006. In Final Form: June 27, 2006

We develop an analytical molecular-thermodynamic model for the aggregation free energy of branching portions of wormlike ionic micelles in 1:1 salt solution. The junction of three cylindrical aggregates is represented by a combination of pieces of the torus and bilayer. A geometry-dependent analytical solution is obtained for the linearized Poisson–Boltzmann equation. This analytical solution is applicable to saddle-like structures and reduces to the solutions known previously for planar, cylindrical, and spherical aggregates. For micellar junctions, our new analytical solution is in excellent agreement with numerical results over the range of parameters typical of ionic surfactant systems with branching micelles. Our model correctly predicts the sequence of stable aggregate morphologies, including a narrow bicontinuous zone, in dependence of hydrocarbon tail length, head size, and solution salinity. For predicting properties of a spatial network of wormlike micelles, our aggregation free energy is used in the Zilman–Safran theory. Our predictions are compared with experimental data for branching micelles of ionic surfactants.

### 1. Introduction

Branched wormlike micelles and spatial networks are found in solutions of both nonionic<sup>1</sup> and ionic<sup>2–13</sup> surfactants and in mixed surfactant systems.<sup>14–17</sup> Micellar branching has a strong effect on the thermodynamic and rheologic behavior of surfactants<sup>2–7,12,13</sup> that find numerous applications,<sup>18–20</sup> for example, in consumer products such as shampoos and cosmetics, and as drug-reducing agents. For various applications, particularly important are ionic surfactants because their behavior can be manipulated by changing pH and salinity.

The occurrence of micellar branching was first suggested by Porte et al.<sup>21</sup> Since then, solutions of branching surfactant micelles have been extensively studied experimentally,<sup>1–11,14–17,22–25</sup> theoretically,<sup>26–30</sup> and by computer simulation.<sup>31,32</sup>

Ionic surfactant systems have been studied by light scattering,<sup>2,3,5,9</sup> small-angle neutron scattering (SANS),<sup>9–11,15,23</sup> cryogenic transmission electron microscopy (cryo-TEM),<sup>6,8,10,11,14,16,24,25</sup> rheological measurements,<sup>2–7,9–11,14,15,23</sup> and by some other techniques.<sup>3,6,23</sup> The addition of salt or an increase of surfactant concentration may cause one-dimensional growth of micelles and produce entangled flexible micelles in solution.<sup>12</sup> Micellar entanglement leads to viscoelastic behavior reminiscent of that observed for solutions of flexible polymers in semidilute regime. Further addition of salt gives a decrease in the viscosity, and eventually the solution phase-separates into viscoelastic and nonviscous phases.<sup>9</sup> This unusual behavior is explained by the formation of connections between wormlike micelles. A connection can slide along the micelle in response to a viscous flow

\* Corresponding author. E-mail: victorov\_a@yahoo.com.

- (1) Bernheim-Groszasser, A.; Wachtel, E.; Talmon, Y. *Langmuir* **2000**, *16*, 4131–4140.
- (2) Appell, J.; Porte, G.; Khatory, A.; Kern, F.; Candau, S. J. *J. Phys. II* **1992**, *2*, 1045–1052.
- (3) Khatory, A.; Kern, F.; Lequeux, F.; Appell, J.; Porte, G.; Morie, N.; Ott, A.; Urbach, W. *Langmuir* **1993**, *9*, 933–939.
- (4) Khatory, A.; Lequeux, F.; Kern, F.; Candau, S. J. *Langmuir* **1993**, *9*, 1456–1464.
- (5) Buhler, E.; Munch, J. P.; Candau, S. J. *J. Phys. II* **1995**, *5*, 765–787.
- (6) Swanson-Vethamuthu, M.; Almgren, M.; Karlsson, G.; Bahadur, P. *Langmuir* **1996**, *12*, 2173–2185.
- (7) Ait Ali, A.; Makhlofi, R. *Colloid Polym. Sci.* **1999**, *277*, 270–275.
- (8) Bernheim-Groszasser, A.; Zana, R.; Talmon, Y. *J. Phys. Chem.* **2000**, *104*, 4005–4009.
- (9) Raghavan, S. R.; Edlund, H.; Kaler, E. W. *Langmuir* **2002**, *18*, 1056–1064.
- (10) Croce, V.; Cosgrove, T.; Maitland, G.; Hughes, T.; Karlsson, G. *Langmuir* **2003**, *19*, 8536–8541.
- (11) Flood, C.; Dreiss, C. A.; Croce, V.; Cosgrove, T.; Karlsson, G. *Langmuir* **2005**, *21*, 7646–7652.
- (12) Magid, L. J. *J. Phys. Chem. B* **1998**, *102*, 4064–4074.
- (13) Shashkina, J. A.; Philippova, O. E.; Zaroslov, Y. D.; Khokhlov, A. R.; Pryakhina, T. A.; Blagodatskikh, I. V. *Langmuir* **2005**, *21*, 1524–1530.
- (14) Lin, Z. *Langmuir* **1996**, *12*, 1729–1737.
- (15) Koehler, R. D.; Raghavan, S. R.; Kaler, E. W. *J. Phys. Chem. B* **2000**, *104*, 11035–11044.
- (16) Bernheim-Groszasser, A.; Zana, R.; Talmon, Y. *J. Phys. Chem. B* **2000**, *104*, 12192–12201.
- (17) Kwon, S. Y.; Kim, M. W. *Phys. Rev. Lett.* **2002**, *89*, 258302–258304.
- (18) Maitland, G. C. *Curr. Opin. Colloid Interface Sci.* **2000**, *5*, 301–311.
- (19) Walker, L. M. *Curr. Opin. Colloid Interface Sci.* **2001**, *6*, 451–456.
- (20) Yang, J. *Curr. Opin. Colloid Interface Sci.* **2002**, *7*, 276–281.

- (21) Porte, G.; Gomati, R.; El Haitamy, O.; Appell, J.; Marignan, J. J. *Phys. Chem.* **1986**, *90*, 5746–5751.
- (22) Bernheim-Groszasser, A.; Tlustý, T.; Safran, S. A.; Talmon, Y. *Langmuir* **1999**, *15*, 5448–5453.
- (23) Schubert, B. A.; Kaler, E. W.; Wagner, N. J. *Langmuir* **2003**, *19*, 4079–4089.
- (24) Danino, D.; Bernheim-Groszasser, A.; Talmon, Y. *Colloids Surf., A* **2001**, *183–185*, 113–122.
- (25) Gonzalez, Y. I.; Kaler, E. W. *Curr. Opin. Colloid Interface Sci.* **2005**, *10*, 256–260.
- (26) Drye, T. J.; Cates, M. E. *J. Chem. Phys.* **1992**, *96*, 1367–1375.
- (27) Cristobal, G.; Rouch, J.; Curely, J.; Panizza, P. *Physica A* **1999**, *268*, 50–64.
- (28) Zilman, A. G.; Safran, S. A. *Phys. Rev. E* **2002**, *66*, 051107–051128.
- (29) Zilman, A.; Tlustý, T.; Safran, S. A. *J. Phys.: Condens. Matter* **2003**, *15*, S57–S64.
- (30) May, S.; Bohbot, Y.; Ben-Shaul, A. *J. Phys. Chem. B* **1997**, *101*, 8648–8657.
- (31) Bohbot, Y.; Ben-Shaul, A.; Granek, R.; Gelbart, W. M. *J. Chem. Phys.* **1995**, *103*, 8764–8782.
- (32) Briels, W. J.; Mulder, P.; den Otter, W. K. *J. Phys.: Condens. Matter* **2004**, *16*, S3965–S3974.

and make possible faster relaxation of stress. A solution of branched micelles is more fluid than a solution of entangled wormlike aggregates.<sup>2,3</sup> Similar behavior is observed in bicontinuous microemulsions that have surprisingly low viscosities while containing a continuous network of aggregated surfactant sheets.<sup>21</sup> Cryo-TEM images clearly show Y-shaped junctions<sup>10,24</sup> between wormlike aggregates with typically three branches.

Drye and Cates<sup>26</sup> proposed a theory that accounts for the entropic gain associated with the formation of micellar junctions and predicts phase separation in solution of branched micelles. The recent statistical mechanical theory of Zilman and Safran<sup>28,29</sup> also shows phase separation and predicts a topological percolation transition, where a micellar network spanning the whole system volume is formed. The key parameters of these theories are the aggregation free energies of the end-cap and the branching portion of a micelle. These aggregation free energies must be specified for a given system before we can apply a micellar network theory.<sup>26–29,33</sup>

The aggregation free energy of a micellar junction was considered by May et al.<sup>30</sup> Their theory predicts an equilibrium shape of a 3-fold junction between wormlike micelles. However, for ionic surfactants, their theory is of limited use because it does not provide an explicit dependence of the electrostatic contribution to the aggregate free energy on solution salinity and the surfactant's molecular parameters.

For ionic surfactant aggregates of spherical, cylindrical, and planar geometries, several molecular-thermodynamic models<sup>34–38</sup> give the aggregation free energy as a function of surfactant tail-length, headgroup size, and solution salinity. For micellar junctions, to the best of our knowledge, there has been no similar model that describes electrostatic interactions and the effect of added electrolyte.

In this work, we develop a molecular-thermodynamic model for the branching portion of an ionic surfactant aggregate. Geometrically, a junction between wormlike micelles is modeled as a union of semitoroidal, planar, and cylindrical surfaces. As in molecular-thermodynamic theories of aggregates of other shapes,<sup>34–38</sup> the free energy is divided into several contributions. The contribution associated with the deformation of hydrophobic tails is estimated from the analytical self-consistent field theory of polymer chains.<sup>34,39,40</sup> The electrostatic contribution is obtained from the linearized Poisson–Boltzmann (PB) theory.

For electrical double layers of arbitrary geometry, a formal solution of the linearized PB equation can be expressed through infinite series.<sup>41</sup> However, there has been no analytical solution in a closed form for a saddle-like surface. For a saddle-like rim of a hole in the planar membrane, an approximate solution has been obtained<sup>42,43</sup> in the limit of zero membrane thickness. This solution incorporates only one of two curvature radii of the rim and requires numerical integration.

## 2. Geometry of a junction

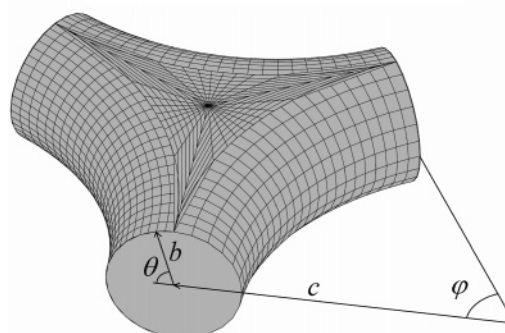


**Figure 1.** Geometry of an aggregate portion that connects three cylindrical micelles.

We obtain an analytical solution for the electric potential by introducing an approximate expression for one-dimensional effective Laplacian<sup>44,45</sup> for a saddle-like part of the junction. A simple analytical expression is obtained for the electrostatic contribution to the free energy of a micellar junction. Our analytical results are compared with the results of the numerical solution of the PB equation in three dimensions.

Our molecular-thermodynamic model is applied to aqueous solutions of ionic surfactants in the presence of 1:1 salt. To calculate the phase behavior and structural properties of a spatial network of branched micelles, we combine our model with the Zilman–Safran theory.<sup>28</sup>

## 2. Geometry of a Junction

The model of a micellar junction<sup>21</sup> is shown in Figure 1. The junction connects three cylindrical semi-infinite micelles and mimics typical cryo-TEM image of micellar junction.<sup>24</sup> The surface of the junction consists of two planar curvilinear triangles enclosed by three saddle-like pieces of the inner surface of the torus. The surface area and the volume of the junction are found by adding contributions of its planar bilayer patch and its semi-torus parts:<sup>46</sup>

$$A_{\text{jun}} = 2c^2\left(\sqrt{3} - \frac{\pi}{2}\right) + \pi b(\pi c - 2b) \quad (1)$$

$$V_{\text{jun}} = 2r_{\text{pl}}c^2\left(\sqrt{3} - \frac{\pi}{2}\right) + \pi b^2\left(\frac{\pi c}{2} - \frac{2b}{3}\right) \quad (2)$$

where  $b$  and  $c$  are the minor and major radii of the torus, and  $2r_{\text{pl}}$  is the thickness of the bilayer patch in the middle of the junction. For the torus, the surface area available to a surfactant molecule,  $a$ , depends on its location on the torus's surface.<sup>30</sup> The average surface area per surfactant molecule in the inner part of the torus is  $a_{\text{tor}} = [(6\pi c - 12b)/(3\pi c - 4b)](v_s/b)$ , where  $v_s$  is surfactant's molecular volume. In the limits  $c \rightarrow 0$  and  $c \rightarrow \infty$ ,  $a_{\text{tor}}$  reduces to the area per molecule for a sphere and cylinder, respectively.

## 3. The Aggregation Free Energy

In this section, we extend previous molecular-thermodynamic models of aggregation<sup>34–38</sup> to micellar junctions. As in molecular-thermodynamic models of rodlike aggregates with spherical

(33) Elleuch, K.; Lequeux, F.; Pfeuty, P. *J. Phys. I* **1995**, 5, 465–474.

(34) Nagarajan, R.; Ruckenstein, E. *Langmuir* **1991**, 7, 2934–2969.

(35) Nagarajan, R.; Ruckenstein, E. In *Equations of State for Fluids and Fluid Mixtures*; Sengers, J. V., Kayser, R. F., Peters, C. J., White, H. J., Eds.; Elsevier Science: Amsterdam, 2000; pp 589–749.

(36) Puvvada, S.; Blankshtein, D. *J. Chem. Phys.* **1990**, 92, 3710–3724.

(37) Goldsipe, A.; Blankshtein, D. *Langmuir* **2006**, 22, 3547–3559.

(38) Bauer, A.; Woelki, S.; Kohler, H.-H. *J. Phys. Chem. B* **2004**, 108, 2028–2037.

(39) Likhtman, A. E.; Semenov, A. N. *Macromolecules* **1994**, 27, 3103–3106.

(40) Milner, S. T. *Macromolecules* **1994**, 27, 2333–2335.

(41) Duplantier, B.; Goldstein, R. E.; Romero-Rochin, V.; Pesci, A. I. *Phys. Rev. Lett.* **1990**, 65, 508–511.

(42) Betterton, M. D.; Brenner, M. P. *Phys. Rev. Lett.* **1999**, 82, 1598–1601.

(43) Fosnaric, M.; Kralj-Iglic, V.; Bohinc, K.; Iglic, A.; May, S. *J. Phys. Chem. B* **2003**, 107, 12519–12526.

(44) Fogolari, F.; Zuccato, P.; Esposito, G.; Viglino, P. *Biophys. J.* **1999**, 76, 1–16.

(45) Victorov, A.; Radke, C.; Prausnitz, J. *Phys. Chem. Chem. Phys.* **2006**, 8, 264–278.

(46) Weisstein, E. W. *CRC Concise Encyclopedia of Mathematics*, 2nd ed.; CRC Press: Boca Raton, FL, 2002.

endcaps and other aggregates of complex shape,<sup>36</sup> we assume additivity of free energies and incompressibility of the aggregate. For micellar junction, the free energy of aggregation is estimated as a combination of contributions from its torus and planar parts:

$$g_{\text{jun}} = \eta_{\text{tor}} g_{\text{tor}} + \eta_{\text{pl}} g_{\text{pl}} \quad (3)$$

where  $g_{\text{jun}}$ ,  $g_{\text{tor}}$ , and  $g_{\text{pl}}$  are the aggregation free energies per surfactant molecule for the entire junction and for its toroidal and planar parts, and  $\eta_{\text{tor}}$  and  $\eta_{\text{pl}}$  are the volume fractions of these parts in the junction, respectively. These volume fractions are calculated from eq 2. To apply eq 3, we need free energy models for the planar and torus aggregates. Below, we formulate such a model for the torus and show its relation to previous results<sup>34</sup> for other aggregate shapes.

For the aggregate of any shape, the aggregation free energy is expressed as the sum of several contributions:<sup>34–38</sup>

$$g = g_{\text{tr}} + g_{\text{int}} + g_{\text{st}} + g_{\text{def}} + g_{\text{el}} \quad (4)$$

where  $g_{\text{tr}}$ ,  $g_{\text{int}}$ ,  $g_{\text{st}}$ ,  $g_{\text{def}}$ , and  $g_{\text{el}}$  are the hydrophobic, the bare interfacial, the polar-head steric repulsion, the tail-deformation, and the electrostatic contributions, respectively. It is the tail-deformation and the electrostatic contribution for toroidal geometry that we propose in this work. The other contributions for aggregates of all shapes are estimated from previous molecular-thermodynamic models,<sup>34–38</sup> as explained below.

The hydrophobic contribution,  $g_{\text{tr}}$ , describes the change in free energy upon transferring the surfactant's hydrocarbon tail from solution to the micelle core.<sup>34–38</sup> The hydrophobic contribution is shape-independent and hence may be discarded when comparing free energies for aggregates of different geometries.

The interfacial contribution,  $g_{\text{int}}$ , is the free energy of the interface between the aggregate hydrocarbon core and the surrounding aqueous solution. The effective area of that interface is equal to the area of the core minus the area shielded by polar headgroups. Thus,<sup>34,36</sup>

$$g_{\text{int}} = \gamma(a - a_0) \quad (5)$$

where  $\gamma$  is the macroscopic interfacial tension between the hydrocarbon core and the surrounding bulk phase, and  $a_0$  is the shielded area per surfactant molecule.

The steric repulsion of headgroups at the interface is described using the repulsion part of the two-dimensional van der Waals equation of state:<sup>34,36</sup>

$$g_{\text{st}} = -kT \ln(1 - a^{\text{eff}}/a) \quad (6)$$

where  $k$  is the Boltzmann constant,  $T$  is the temperature, and  $a^{\text{eff}}$  is the effective cross-section of the surfactant's headgroup.

The analytical expression for the free energy of deformation of surfactant tails in the aggregate,  $g_{\text{def}}$ , is obtained from the analytical self-consistent field theory of chainlike molecules in the strong-segregation limit.<sup>39,40</sup> For Gaussian chains, the potential of the effective field acting on chain segments is quadratic in the distance from the aggregate surface. The elastic free energy of surfactant tails is estimated by integrating this parabolic field over the aggregate core.<sup>39</sup> For torus elements of a junction, we have

$$\frac{g_{\text{def}}}{kT} = \frac{3\pi^2}{8NL^2V_{\text{tor}}} \int_0^\pi d\varphi \int_{\pi/2}^{3\pi/2} d\theta \int_0^b (b-r)^2 r(c+r \cos \theta) dr \quad (7)$$

where  $r(c+r \cos \theta)$  is the Jacobian in the coordinate system A1 that we introduce in Appendix A for describing the torus geometry,  $V_{\text{tor}}$  is the volume of the torus parts of the junction (see Figure 1),  $L$  is the Kuhn segment length, and  $N = l_s/L$  is the number of segments in the chain of a contour length  $l_s$ . Integration in eq 7 gives

$$\frac{g_{\text{def}}}{kT} = B \frac{\pi^2}{80N} \left(\frac{b}{L}\right)^2 \quad (8)$$

where  $B = (15\pi c - 12b)/(3\pi c - 4b)$ . For  $c \rightarrow 0$  and  $c \rightarrow \infty$ , we obtain  $B = 3$  and  $B = 5$ , respectively, and eq 8 reproduces the results known previously for spheres and cylinders,<sup>34</sup> where  $b$  is equal to  $r_{\text{sph}}$  or to  $r_{\text{cyl}}$ . For a plane,<sup>34</sup>  $B = 10$  and  $b = r_{\text{pl}}$ .

The electrostatic contribution of eq 4,  $g_{\text{el}}$ , is estimated from the solution of the linearized PB equation. For the complex geometry shown in Figure 1, the linearized PB equation can only be solved numerically. To obtain analytic expressions for the electric potential, we reduce the initial three-dimensional problem to an effective one-dimensional case by introducing an approximate angle-averaged Laplacian (Appendix A). The boundary conditions are a vanishing electric field far from the aggregate and the Gauss law at the aggregate surface. The solution of the linearized PB equation is (Appendix A):

$$u(x) = t \left(\frac{x_0}{x}\right)^p \frac{K_p(x)}{K_{p+1}(x_0)} \quad (9)$$

where

$$t = \frac{4\pi l_B}{ek} \sigma \quad (10)$$

$$p = (m-1)/2 \text{ and } m = \frac{c + 2b \cos \theta^*}{c + b \cos \theta^*} \quad (11)$$

Here,  $u = e\Psi/kT$  is the reduced electric potential,  $\Psi$  is the electric potential,  $e$  is the elementary positive charge,  $\sigma = q/a$  is the surface charge density,  $q$  is the aggregate charge per surfactant molecule,  $\kappa = (8 \times 10^3 \pi N_A l_B C_{\text{salt}})^{1/2}$  is the inverse Debye length,  $l_B = e^2/4\pi\epsilon\epsilon_0 kT$  is the Bjerrum length,  $C_{\text{salt}}$  is the molar concentration of 1:1 salt,  $N_A$  is Avogadro's number,  $\epsilon$  is the dielectric permittivity of the medium,  $\epsilon_0$  is the dielectric permittivity of free space,  $x = r\kappa$  is the reduced distance,  $x_0 = b\kappa$  is the coordinate of the surface,  $K_\nu(x)$  is the modified Bessel function of the second kind of order  $\nu$  (see ref 47, p 709), and  $\theta^*$  is an effective angle between  $\pi/2$  and  $\pi$  (Appendix A). This angle describes an effective average orientation of vector  $\mathbf{b}$ , Figure 1, in the semi-torus element of the junction. As shown below, good results are obtained for  $\theta^* = 3\pi/4$ . We use this value for  $\theta^*$  when not stated otherwise. For spheres and cylinders, we have  $c \rightarrow 0$  and  $c \rightarrow \infty$ , respectively. This gives  $m = 2$  and  $m = 1$ , and eq 9 becomes exact for the limiting cases of spherical and cylindrical geometry. Equation 9 reduces to previously known results:<sup>48</sup>  $u(x) = t[x_0^2/(1+x_0)][(\exp(x_0-x))/x]$  for a sphere ( $m = 2$ ),  $u(x) = t[K_0(x)]/[K_1(x_0)]$  for a cylinder ( $m = 1$ ), and  $u(x) = t \exp(x_0 - x)$  for a plane ( $m = 0$ ).

The analytic expression for the electrostatic free energy of semi-toroidal, spherical, cylindrical, and planar aggregates is obtained by integrating the surface value of the electric potential,

(47) Arfken, G. B.; Weber, H. J. *Mathematical Methods for Physicists*, 5th ed.; Academic Press: London, 2001.

(48) Winterhalter, M.; Helfrich, W. *J. Phys. Chem.* **1988**, *92*, 6865–6867.



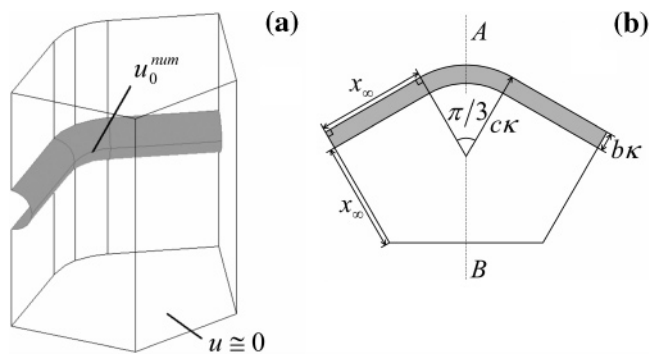


**Figure 2.** (a) Micellar cell used for the numerical solution of the PB equation. The cell contains one of the three identical elements of a micellar junction (shaded) in the surrounding solution. (b) Cross-section of the cell by the plane that contains long axes of cylindrical micelles.  $b$  and  $c$  are the minor and the major radii of the torus part of micellar junction,  $\kappa^{-1}$  is the Debye length, and  $x_\infty$  is the size of the cell.  $AB$  is the axis of symmetry.

eq 9, over the charge density<sup>49–51</sup> (see Appendix C). The result of integration is

$$\frac{g_{el}}{kT} = \frac{a\kappa}{8\pi l_B K_{p+1}(x_0)} t^2 \quad (12)$$

Combining eqs 4–6, 8, and 12, we calculate the aggregation free energy for an aggregate of specified shape and curvature radii at a given temperature and solution salinity. The length and the volume of a fully extended  $n$ -alkyl tail of a surfactant molecule are calculated as suggested by Tanford:<sup>52</sup>  $l_s = 0.15 + 0.1265n_C$  [nm] and  $v_s = 0.0274 + 0.0269n_C$  [nm<sup>3</sup>], respectively, where  $n_C$  is the number of carbon atoms in the hydrocarbon chain. The Kuhn segment length is  $L = 0.46$  nm, and the cross-section of a hydrocarbon chain is  $a_0 = L^2$ .<sup>34</sup> Correlations for calculating  $\gamma$  and  $\epsilon$  are taken from ref 34. Thus, the individual molecular parameters of surfactant are the number of carbon atoms in a surfactant's tail,  $n_C$ , and the effective cross-section of its head,  $a^{\text{eff}}$ .

#### 4. Numerical Solution of the PB Equation

The electric potential derived in the previous section gives the exact solution of the linearized PB equation for aggregates of spherical, cylindrical and planar geometries in 1:1 salt solution. For aggregates of torus-like geometry, our analytical result is approximate because it is the solution of the linearized PB equation in its approximate form, obtained by simplifying the initial three-dimensional Laplacian in this equation.

To test the analytical expressions for the electric potential and for the free energy of a torus-like aggregate surface, eqs 9 and 12, we numerically solved the initial three-dimensional linearized PB equation,  $\nabla^2 u = u$ . We used FEMLAB 2.3, the finite-element method software for solving partial differential equations. Figure 2 shows the micellar cell used in the calculations. This cell contains one of the three identical elements of the junction depicted in Figure 1. The gray portion is the aggregate surface: two semi-infinite cylinders are connected through the torus's element. The electrolyte solution is everywhere around the aggregate. We assume a uniform surface charge density of the curved aggregate. The boundary conditions are the Gauss law,  $\nabla u \cdot \vec{n} = -t$ , for the

aggregate surface, and  $\nabla u \cdot \vec{n} = 0$  for the cell external boundaries, where  $\vec{n}$  is the unit normal to these surfaces. The size of the cell,  $x_\infty$ , is adjusted to ensure vanishing electric potential  $u$  in the bulk solution far from the aggregate.

From the numerical results on the spatial distribution of the electric potential,  $u(\vec{x})$ , we calculate the electrostatic free energy of the cell,  $\Omega_{\text{cell}}$  (see Appendix B, eq B14):

$$\frac{\Omega_{\text{cell}}}{kT} = \frac{1}{8\pi l_B \kappa} \int_V [(\nabla u)^2 + u^2] d\vec{x} \quad (13)$$

where  $\vec{x}$  is the spatial variable in units of reduced length:  $\vec{x} = \kappa \vec{r}$ .

The electrostatic free energy of the saddle-like toroidal part of the junction,  $\Omega_{\text{tor}}$ , is obtained as

$$\Omega_{\text{tor}} = \Omega_{\text{cell}} - \Omega_{\text{cyl}} \quad (14)$$

where  $\Omega_{\text{cyl}}$  is the free energy of the cylindrical parts of the aggregate in the cell. The free energy of a cylinder of radius  $x_0 = b\kappa$  and length  $x_\infty$  is calculated from the exact analytical result, eq 12.

For calculating the free energy from our analytical potential, we use two different approximations: (1) apply eq 12 with a constant effective angle  $\theta^* = 3\pi/4$  (upper index I), and (2) integrate the analytic electric potential, eq 9, over the torus's surface using the angular  $\theta^*$  dependence (upper index II) that enters the potential through the indexes of the Bessel functions. Thus, the deviations between numerical and analytical free energies are calculated from

$$\delta\Omega^I = (\Omega^I - \Omega_{\text{tor}})/\Omega_{\text{tor}} \quad (15)$$

$$\delta\Omega^{II} = (\Omega^{II} - \Omega_{\text{tor}})/\Omega_{\text{tor}} \quad (16)$$

Here,  $\Omega_{\text{tor}}$  is the FEMLAB numerical value obtained from eqs 13 and 14;  $\Omega^I = n_{\text{tor}} g_{el}$ , where  $n_{\text{tor}}$  is the aggregation number of the toroidal part of the junction, and  $g_{el}$  is calculated from eq 12;  $\Omega^{II}$  is obtained substituting eq 9 into eq C2 (Appendix C):

$$\frac{\Omega^{II}}{kT} = \frac{1}{8\pi l_B \kappa} \left[ t^2 x_0^2 \int_0^{\pi/3} d\varphi \int_{\pi/2}^{3\pi/2} \frac{K_{p(\theta^*)}(x_0)}{K_{p(\theta^*)+1}(x_0)} \left( \frac{c}{b} + \cos \theta^* \right) d\theta^* \right] \quad (17)$$

The reduced electrostatic potential  $u(\vec{x})$  is determined by specifying the reduced charge density,  $t$ , the reduced minor radius of the aggregate surface,  $x_0 \equiv b\kappa$ , and the ratio  $c/b$ . A given set of these parameters may correspond to different physical situations, that is, to infinitely many combinations of charge density, salt concentration, and aggregate size. Below, we compare the numerical and analytical results within the interval of parameter values that is important for branching micelles of ionic surfactants. The salinity is in the range 1 mM to 1 M,  $b$  changes from  $\sim 1$  to 2.5 nm, and the charge density is up to one fully charged headgroup per 0.5 nm<sup>2</sup>. These values are typical of ionic surfactants with a tail length  $n_C$  between 10 and 22.

Our numerical and analytical results are given in Figures 3–5 and in Table 1. Figures 3–5 show the spatial distribution of the electric potential. Table 1 contains the electrostatic free energies calculated from eqs 13–14 and the electric potential calculated by FEMLAB on the surface of the aggregate,  $u_0^{\text{num}}$ , in the center of the torus-like element ( $r = b$ ,  $\theta = \pi$ ,  $\varphi = \pi/6$ ), as shown in Figure 2. In Table 1, also given are the relative deviations between

(49) Derjaguin, B. V. *Trans. Faraday Soc.* **1940**, 35, 203–215.

(50) Verwey, E. J. W.; Overbeek, J. T. G. *Theory of the Stability of Lyophobic Colloids*; Dover: Mineola, NY, 1948.

(51) Derjaguin, B. V. *Usp. Khim. SSSR* **1979**, 48, 675–721.

(52) Tanford, C. *The Hydrophobic Effect: Formation of Micelles and Biological Membranes*, 2nd ed.; Wiley: New York, 1980.

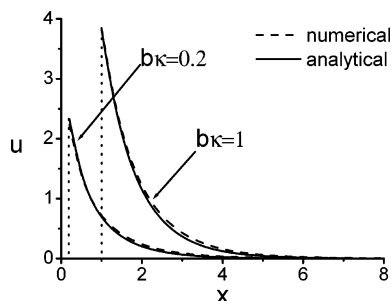


**Figure 3.** Dependence of the reduced electric potential on the reduced distance from the aggregate along the vertical axis of symmetry of Figure 2b ( $\theta = \pi$ ,  $\varphi = \pi/6$ ). Dotted lines show the position of the charged aggregate surface. The ratio of the torus radii is  $c/b = 5$ ; the reduced charge density  $t = 5$  (see eq 10). Results are given for two values of the torus's reduced radius,  $b\kappa$ .

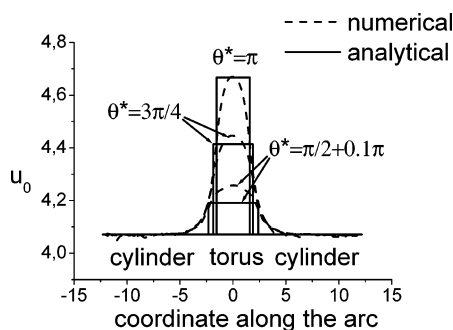


**Figure 4.** Profiles of the electric potential on the junction surface as we move along the arcs shown in Figure 2b from the left cylinder to the right cylinder. The coordinate along the arc is given in units of  $\kappa^{-1}$ . The zero of this coordinate is at the axis of vertical symmetry of Figure 2b. Angle  $\theta^*$  specifies the location of arcs on the junction surface:  $\theta^* = \pi/2$  and  $\theta^* = \pi$  for the upper and lower arcs shown in Figure 2b, respectively. For an intermediate parallel arc,  $\theta^* \in (\pi/2, \pi)$ . The results are given for  $c/b = 2.5$ ,  $t = 5$  (see eq 10), and  $b\kappa = 2$ .

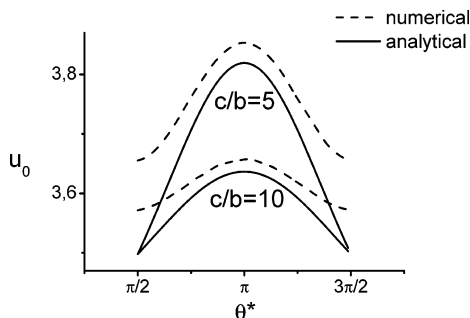


**Figure 5.** Profile of the surface electric potential in the middle of the torus element of the junction as we move around the torus from its top at  $\theta^* = \pi/2$  to its bottom at  $\theta^* = 3\pi/2$ .  $\theta^* = \pi$  specifies the point on the torus surface, labeled  $u_0^{\text{num}}$  in Figure 2a. Calculation is performed for  $t = 5$  and  $b\kappa = 1$ .

the numerical and analytical results. The results are shown for  $t = 5$ . For changing solution salinity, this gives surface charge densities that range from  $\sim 17 \text{ nm}^2$  per charge at  $C_{\text{salt}} = 1 \text{ mM}$  to  $\sim 0.5 \text{ nm}^2$  per charge at  $C_{\text{salt}} = 1 \text{ M}$ . Table 1 shows that the reduced surface potential in this interval of salinities and charge densities is greater than unity, that is, it is formally outside the range of applicability of the linear PB theory. However, numerical analysis shows<sup>44,53</sup> that the nonlinear and linearized versions of the PB equation give close results up to reduced potentials of

about 3–4 for charged particles of different shape in a similar interval of particle sizes and solution salinities. The reduced charge density  $t$  does not affect the relative error for the surface potential and for the free energy. This is because, in the linearized PB theory, the electric potential depends linearly on the charge density, and, for the free energy, this dependence is quadratic.

The first column of Table 1 gives the reduced minor radius of the torus. Each value corresponds to various combinations of radius  $b$  and salt concentration,  $C_{\text{salt}}$ . The second column shows  $C_{\text{salt}}$  for  $b = 1.5 \text{ nm}$ , a typical thickness of wormlike micelles for  $C_{12}$ – $C_{16}$  surfactants. For junctions, the optimal value of  $c/b$  is typically 5–6, as obtained in the next section. Nevertheless, in Table 1, we give results for a much broader range of  $c/b$  values to assess our analytical approximation for a variety of geometries.

Table 1 shows that, at a given  $b\kappa$ , the relative errors in the surface potential and free energy decrease with  $c/b$ . For typical junction values of  $c/b$ , the agreement between the analytical and numerical results is remarkably good, except at a low salinity of about 1 mM. Branching of ionic micelles is normally observed at much higher salinities (100–1500 mM),<sup>3,4,9–11</sup> where our model is reliable.

Figure 3 shows profiles of the electric potential as we move away from the charged aggregate into the bulk solution. The agreement between the numerical and analytical solutions is excellent.

Shown in Figure 4 are profiles of the electric potential on the aggregate surface as we move along one cylindrical branch of the aggregate, pass the junction, and arrive at another cylindrical branch. The potential is higher on the torus's surface than on the neighboring cylinders. Far from the junction, the potential reduces to that of an infinite cylinder. Stepwise potentials are analytical results (eq 9) for several effective angles  $\theta^*$ . Figure 4 shows that our theory gives quite reasonable average surface potentials for the junction. For  $\theta^* = 3\pi/4$ , the predicted potential is somewhat too high in the intermediate parts of the junction and somewhat too low in its middle and terminal zones. Because the free energy is an integral of the potential over the whole surface of the junction, the inaccuracies of the analytical potential tend to cancel out, leading to small errors,  $\delta\Omega^I$  (see Table 1).

Figure 5 shows variation in the surface potential as we move around the middle part of the junction from its planar top to its bottom. The analytical results are given as a function of the effective angle  $\theta^*$ . The  $\theta^*$  dependence of our analytic potential correctly mimics the actual  $\theta$  dependence of the numerical result. This supports the introduction of the effective parameter  $\theta^*$  for approximating the Laplacian, eq A4 (Appendix A).

The angular  $\theta^*$  dependence of the analytic potential is used in eq 17 for the free energy,  $\Omega^{\text{II}}$ . Deviations  $\delta\Omega^{\text{II}}$  are close to  $\delta\Omega^I$  (see Table 1), suggesting that eq 12 with constant  $\theta^* = 3\pi/4$  is a good analytical approximation for the electrostatic free energy.

## 5. Aggregates of Optimal Size and Shape

For spherical, cylindrical, and planar aggregates, the optimal size was found by minimizing their free energies,  $g_{\text{sph}}(r_{\text{sph}})$ ,  $g_{\text{cyl}}(r_{\text{cyl}})$ , and  $g_{\text{pl}}(r_{\text{pl}})$ , with respect to  $r_i$  ( $i = \text{sph, cyl, pl}$ ) under the constraint  $r_i \leq l_s$ , where  $l_s$  is the length of a fully extended surfactant tail. For the junction,  $g_{\text{jun}}(b, c, r_{\text{pl}})$  was minimized with respect to  $b$  and  $c$  under the constraints  $b \leq l_s$  and  $b < c$ . The width of the planar part of the junction was set equal to the width of an optimal infinite bilayer,  $r_{\text{pl}} = r_{\text{pl}}^*$ . Subsequent minimization of  $g_{\text{jun}}(b, c, r_{\text{pl}})$  with respect to all three parameters gives insignificant change in the free energy.

The optimal geometry of the junction and the sequence of free energies for aggregates of different shapes depend on the solution

**Table 1. Numerical and Analytical Results for the Surface Potential and the Electrostatic Free Energy of the Torus Part of the Micellar Junction<sup>a</sup>**

| $b/c$ | $C_{\text{salt}}$<br>(mM) | $c/b$ | $u_0^{\text{num}}$ | $\delta u_0$<br>(%) | $8\pi l_{\text{BK}}[\Omega_{\text{tor}}/(kT)]$ | $\delta\Omega^I$<br>(%) | $\delta\Omega^{II}$<br>(%) | $u_{\text{res}}^{\text{max}}$ | $x_{\infty}$ |
|-------|---------------------------|-------|--------------------|---------------------|--|-------------------------|----------------------------|-------------------------------|--------------|
| 3     | 369                       | 10    | 4.387              | 0.2                 | 6050   | 0.2                     | 0.1                        | $6 \cdot 10^{-8}$             | 20           |
|       |                           | 5     | 4.507              | -0.5                | 2856   | 0.2                     | -0.1                       | $1 \cdot 10^{-8}$             | 20           |
|       |                           | 3     | 4.685              | -0.8                | 1582   | 0.0                     | -0.5                       | $8 \cdot 10^{-9}$             | 20           |
|       |                           | 2     | 4.996              | 0.1                 | 947.6  | -0.3                    | -1.3                       | $1 \cdot 10^{-6}$             | 15           |
|       |                           | 1.5   | 5.373              | 7.6                 | 633.2  | -0.6                    | -2.4                       | $1 \cdot 10^{-6}$             | 15           |
| 2     | 164                       | 10    | 4.172              | -0.2                | 2548   | 0.0                     | -0.2                       | $1 \cdot 10^{-6}$             | 15           |
|       |                           | 5     | 4.312              | -0.6                | 1212   | -0.3                    | -0.6                       | $8 \cdot 10^{-7}$             | 15           |
|       |                           | 3     | 4.542              | -0.7                | 679.4  | -0.7                    | -1.5                       | $7 \cdot 10^{-7}$             | 15           |
|       |                           | 2     | 4.873              | 2.6                 | 415.1  | -1.6                    | -3.0                       | $8 \cdot 10^{-7}$             | 15           |
|       |                           | 1.5   | 5.215              | 18                  | 285.0  | -2.5                    | -4.8                       | $7 \cdot 10^{-7}$             | 15           |
| 1     | 41.0                      | 10    | 3.657              | -0.6                | 556.7  | -0.6                    | -0.9                       | $5 \cdot 10^{-7}$             | 15           |
|       |                           | 5     | 3.854              | -0.9                | 270.7  | -1.7                    | -2.3                       | $8 \cdot 10^{-5}$             | 10           |
|       |                           | 3     | 4.109              | 1.6                 | 157.3  | -3.6                    | -4.8                       | $8 \cdot 10^{-5}$             | 10           |
|       |                           | 2     | 4.390              | 14                  | 101.5  | -6.1                    | -8.1                       | $8 \cdot 10^{-5}$             | 10           |
|       |                           | 1.5   | 4.633              | 54                  | 74.13  | -7.9                    | -10                        | $8 \cdot 10^{-5}$             | 10           |
| 0.5   | 10.2                      | 10    | 3.007              | -1.2                | 114.8  | -2.3                    | -2.8                       | $5 \cdot 10^{-5}$             | 10           |
|       |                           | 5     | 3.216              | 0.0                 | 58.19  | -5.6                    | -6.5                       | $5 \cdot 10^{-5}$             | 10           |
|       |                           | 3     | 3.424              | 8.6                 | 35.95  | -10                     | -12                        | $5 \cdot 10^{-5}$             | 10           |
|       |                           | 2     | 3.615              | 38                  | 25.07  | -15                     | -17                        | $5 \cdot 10^{-5}$             | 10           |
|       |                           | 1.5   | 3.854              | 110                 | 17.1   | -28                     | -30                        | $3 \cdot 10^{-5}$             | 10           |
| 0.2   | 1.64                      | 10    | 2.089              | -2.5                | 13.16  | -7.8                    | -8.5                       | $2 \cdot 10^{-5}$             | 10           |
|       |                           | 5     | 2.237              | 4.0                 | 7.310  | -16                     | -17                        | $2 \cdot 10^{-5}$             | 10           |
|       |                           | 3     | 2.355              | 27                  | 5.028  | -24                     | -26                        | $2 \cdot 10^{-5}$             | 10           |
|       |                           | 2     | 2.450              | 110                 | 3.911  | -28                     | -30                        | $3 \cdot 10^{-5}$             | 10           |
|       |                           | 1.5   | 2.615              | 277                 | 2.854  | -33                     | -33                        | $2 \cdot 10^{-5}$             | 10           |
| 0.15  | 0.92                      | 10    | 1.816              | -2.7                | 6.572  | -10                     | -11                        | $2 \cdot 10^{-5}$             | 10           |
|       |                           | 5     | 1.939              | 6.1                 | 3.785  | -20                     | -22                        | $2 \cdot 10^{-5}$             | 10           |
|       |                           | 3     | 2.034              | 35                  | 2.701  | -29                     | -31                        | $2 \cdot 10^{-5}$             | 10           |
|       |                           | 2     | 2.109              | 140                 | 2.162  | -33                     | -33                        | $2 \cdot 10^{-5}$             | 10           |

<sup>a</sup>  $u_0^{\text{num}}$  is the electric potential at the center of the junction (see Figure 2a), from the numerical solution of the linearized PB equation; obtained from this solution and eqs 13–14 is the electrostatic free energy of the toroidal part of the junction,  $\Omega_{\text{tor}}$ .  $\delta\Omega^I$ ,  $\delta\Omega^{II}$ , and  $\delta u_0 = (u_0^{\text{anal}} - u_0^{\text{num}})/u_0^{\text{num}}$  are relative deviations between the numerical and analytical results;  $b$  and  $c$  are the minor and major radii of torus, respectively;  $x_{\infty}$  is the size of the micellar cell (see Figure 2b);  $u_{\text{res}}^{\text{max}}$  is the maximum FEMLAB value of the electric potential on the cell boundary that opposes the aggregate (see Figure 2a).

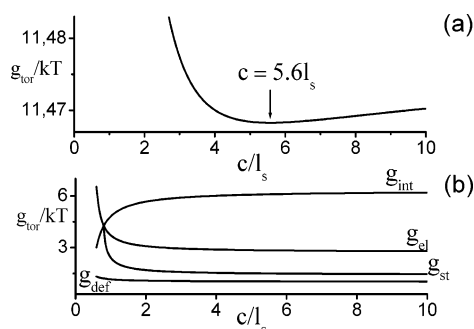


**Figure 6.** (a) Free energy of a torus element of the junction as a function of the major radius  $c$  (in units of the length of the fully extended surfactant tail,  $l_s$ ). The arrow shows a minimum of  $g_{\text{tor}}$ . Shape-independent hydrophobic contribution is omitted from  $g_{\text{tor}}$ . (b) The interfacial,  $g_{\text{int}}$ , steric,  $g_{\text{st}}$ , electrostatic,  $g_{\text{el}}$ , and deformation,  $g_{\text{def}}$ , contributions to the free energy of the torus versus its major radius. The results are shown for CTAB at  $T = 298$  K,  $C_{\text{KBr}} = 350$  mM. Model parameters are  $n_c = 16$ ,  $a^{\text{eff}} = 0.54$  nm<sup>2</sup>, and  $b = 0.6l_s$ , which is the minor radius of the optimal torus.

salinity. At low salt concentrations, the free energy of the toroidal part of the junction,  $g_{\text{tor}}(b, c)$ , is a monotonically decreasing function of  $c$ . Because at large  $c$  we have  $g_{\text{tor}}(b, c \rightarrow \infty) = g_{\text{cyl}}(b)$ , the cylinders are more stable than the aggregates of torus geometry at low salt concentrations. For higher salinity, a minimum of  $g_{\text{tor}}(b, c)$  appears at finite  $c$ . This minimum is shown in Figure 6, which illustrates the  $c$  dependence of  $g_{\text{tor}}$  and its different contributions. The interfacial contribution,  $g_{\text{int}}$ , increases with  $c$  and becomes constant at large  $c$ . This is because, in the torus, the average area per molecule increases with  $c$ , approaching its limiting value for a cylinder. The steric, electrostatic, and deformation contributions decrease with  $c$ . A small change in

the contributions to  $g_{\text{tor}}$  is sufficient to cause a shift or disappearance of the shallow minimum shown in Figure 6a. Thus, our model reflects the sensitivity of the response typical of soft self-assembling systems that show rich structural behavior.

For the torus piece of the junction, the optimal  $c$  decreases with salt concentration. However, for the junction as a whole, including its planar patch, we have a different dependence of the optimal  $c$  on salinity. In the high-salt limit, the lamellae have the lowest free energy. Therefore, at high salinity, the size of the planar element of the junction increases and starts to dominate in the junction free energy. The growth of the junction's planar element implies an increase in  $c$ . At large  $c$ , the free energy of the junction reduces to that of a planar aggregate:  $g_{\text{jun}}(r_{\text{pl}}, b, c \rightarrow \infty) = g_{\text{pl}}(r_{\text{pl}})$ , as we see from eqs 1, 2, and 3. Thus, at high salinity,  $g_{\text{jun}}(r_{\text{pl}}, b, c)$  is a decreasing function of  $c$ , and the junctions are unstable with respect to infinite planar aggregates. At lower salinity,  $g_{\text{jun}}(r_{\text{pl}}, b, c)$  has a minimum at finite  $c$ .

Figure 7 shows the sequence of aggregate geometries predicted by our model for cetyltrimethylammonium bromide (CTAB) in an aqueous solution of KBr. The molecular parameters are taken from ref 35. At low salt concentration, spherical aggregates have the lowest free energy, and the solution contains only spherical micelles. As the salinity increases, the cylinder becomes more stable than the sphere, inducing one-dimensional growth of the aggregates. At a higher salt content, the cylinder remains the most stable geometry, but the free energy of the junction becomes lower than that of the spherical endcap of a wormlike aggregate. This causes branching of wormlike aggregates and the formation of a spatial network in solution. Planar geometry has the lowest free energy in the high-salt limit. Hence, the lamellae phase becomes stable at high solution salinity. The inset of Figure 7



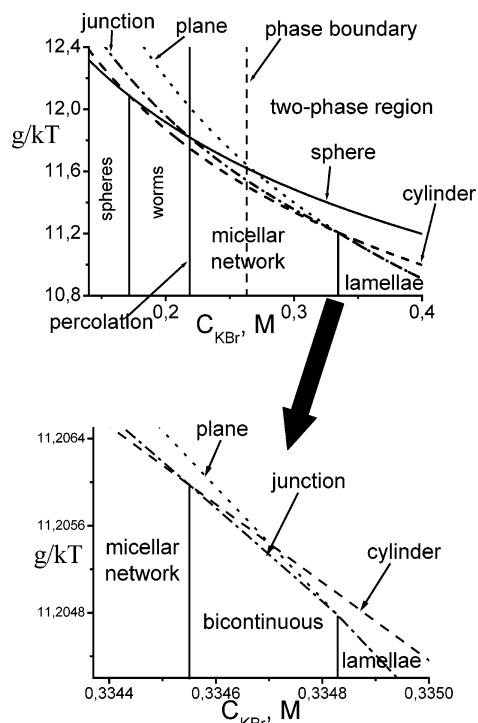


**Figure 7.** Aggregation free energy versus salinity for an aqueous solution of CTAB+KBr. The inset shows a narrow region of stable junctions that corresponds to bicontinuous morphology. Shape-independent hydrophobic contribution is not included in  $g$ .  $n_c = 16$ ,  $a^{\text{eff}} = 54 \text{ nm}^2$ ,<sup>34,35</sup>  $T = 308 \text{ K}$ ; percolation and phase transitions are calculated for  $C_{\text{CTAB}} = 0.35 \text{ M}$ .

shows a narrow region of salt concentration where junction geometry is the most stable one. This region is between the domains of stable cylinder networks and stable planar aggregates and corresponds to spongelike bicontinuous structures. A previous molecular theory of micellar junctions<sup>30</sup> predicts no stable bicontinuous morphology. At the level of approximations of our model, the differences in the free energies of competing structures, shown in the inset of Figure 7, are definitely too small to give a reliable prediction of the bicontinuous phase. However, our model shows that bicontinuous structures are likely to form in this region and are also likely to disappear upon minor change of conditions. This is in line with the very narrow zone observed for bicontinuous structures in many surfactant and block-copolymer systems.

For a range of surfactant molecular parameters, our model predicts aggregate stability maps similar to that shown in Figure 7. While these maps agree qualitatively with the experiment for network-forming ionic surfactants, the results are quantitatively very different for specific systems. Thus, for CTAB+KBr, the micellar network is found at a much higher salt concentration ( $\sim 1.5 \text{ M}$ )<sup>4</sup> than shown in Figure 7. A better prediction of the onset of the network is obtained for a solution of erucylbis-(hydroxyethyl)methylammonium chloride (EHAC) with added KCl, while, for EHAC+NaCl, the results are quite good, as shown in the next section. The quality of predicting the sphere-to-rod transition also varies from system to system. For example, in EHAC+KCl, this transition is predicted at  $0.15 \text{ M}$  KCl. This is close to the experimental value of  $0.2 \text{ M}$  found from SANS and cryo-TEM measurements.<sup>10</sup> In CTAB+KBr, the predicted transition is at  $0.17 \text{ M}$  KBr versus  $\sim 0.1 \text{ M}$  KBr in experiment.<sup>58</sup> However, the results can be also much less accurate, as explained below.

For sphere-to-rod, rod-to-network, and network-to-lamellae transitions, the model predicts a decrease in solution salinity at

the transition point upon increasing the length of the surfactant tail or decreasing the size of the headgroups. However, this dependence of transition points on the surfactant's molecular structure is noticeably weaker than that found experimentally for sphere-to-rod transitions of halide ammonium salts ( $\text{C}_n\text{H}_{2n+1}\text{N}(\text{CH}_3)_m\text{H}_3\text{-mCl}$  and  $\text{C}_n\text{H}_{2n+1}\text{N}(\text{CH}_3)_m\text{H}_3\text{-mBr}$ ;  $m = 0, 2, 3$ ;  $n = 12, 14, 16$ ).<sup>54–58</sup> The deviation from the experimental dependence of the transitions on tail length may be attributed to approximations in the model chain-packing term,  $g_{\text{def}}$ . Taking into account more structural details of micelle coronas (than those reflected by  $g_{\text{int}}$  and  $g_{\text{st}}$  in their present form) would help to improve the description of the effect of the surfactant head.

Experiment shows strong specific anion effects on morphology-transition points. For example, changing Br to Cl in tetradecyltrimethylammonium salt shifts the sphere-to-rod transition from  $120 \text{ mM}$  to  $2.7 \text{ M}$ .<sup>55</sup> As with other theories that do not take into account the specific ion effects,<sup>34–36</sup> our model fails to explain more than a 10-fold difference of the salinity at the sphere-to-rod transition for alkyltrimethylammonium bromides<sup>55,57,58</sup> and chlorides.<sup>55,56</sup> Because our model does not account for the specific ion effects, it also cannot reflect substantial differences observed for the onset of a network, as shown below.

## 6. Spatial Networks of Branching Micelles

Our model gives the free energy of a single aggregate in solution. To describe the thermodynamic and structural properties of an assembly of aggregates, we need a theory that relates these properties to the aggregation free energy. The dilute-solution approximation that has been used in several molecular-thermodynamic theories of aggregation<sup>34–38</sup> is not applicable to solutions of wormlike aggregates that may form spatial networks. Here, we use the Zilman and Safran<sup>28</sup> theory, which exploits the analogy between wormlike micelles and polymer chains.<sup>59</sup> In this theory, the wormlike micelle is a sequence of basic units called “monomers”. Physically these monomers are interpreted as minimal micelles that exist in surfactant solution.<sup>28,59</sup> The role of true surfactant monomers is negligible at this level of description, which considers the aggregation equilibrium between minimal micelles and wormlike micellar chains composed of these building blocks. The monomers are arranged on a lattice with a coordination number,  $z_c$ . The micellar network is a collection of micellar chains that have defects: branching points and end-caps. The volume fractions of these branching points,  $\phi_j$ , and end-caps,  $\phi_e$ , are given by<sup>28</sup>

$$\phi_j = \alpha(2\phi/z_c)^{3/2} \exp(-n_{\text{mon}}(g_{\text{jun}} - g_{\text{cyl}})/kT) \quad (18)$$

$$\phi_e = (2\phi/z_c)^{1/2} \exp(-n_{\text{mon}}(g_{\text{sph}} - g_{\text{cyl}})/kT) \quad (19)$$

where  $\phi$  is the total volume fraction of monomers, which is approximately equal to the volume fraction of surfactant when the system is well above its critical micelle concentration;  $n_{\text{mon}}$  is the aggregation number of a minimal micelle;  $\alpha$  is the lattice parameter;  $g_{\text{sph}}$ ,  $g_{\text{cyl}}$ , and  $g_{\text{jun}}$  are the aggregation free energies for the aggregates of different shape. The average length of the micellar chain between two defects (junction or end) in the units of the monomer's length is

(54) Ikeda, S.; Ozeki, S.; Tsunoda, M.-A. *J. Colloid Interface Sci.* **1980**, *73*, 27–37.

(55) Imae, T.; Ikeda, S. *J. Phys. Chem.* **1986**, *90*, 5216–5223.

(56) Imae, T.; Abe, A.; Ikeda, S. *J. Phys. Chem.* **1988**, *92*, 1548–1553.

(57) Ozeki, S.; Ikeda, S. *J. Colloid Interface Sci.* **1982**, *87*, 424–435.

(58) Imae, T.; Kamiya, R.; Ikeda, S. *J. Colloid Interface Sci.* **1985**, *108*, 215–225.

(59) Wang, Z. G.; Costas, M. E.; Gelbart, W. M. *J. Phys. Chem.* **1993**, *97*, 1237–1242.



$$l_{av} = \frac{2\phi}{3\phi_j + \phi_e} \quad (20)$$

The free energy of the system per lattice site is<sup>28</sup>

$$f/kT = (1 - \phi) \ln(1 - \phi) - \phi_e - \phi_j \quad (21)$$

The theory of Zilman and Safran predicts phase separation of a network-forming micellar solution, and it also predicts a nonthermodynamic percolation transition. The percolation transition takes place when  $3\phi_j = \phi_e$ . The coexistence line is found by equating the chemical potentials and the osmotic pressure in both phases.

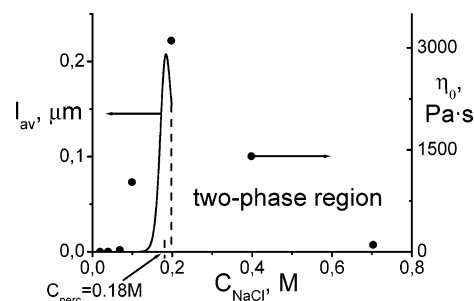
In this work, we took the optimal spherical aggregate as the minimal micelle. Hence,  $n_{mon} = V_{sph}/v_s$ , where  $V_{sph}$  is the volume of the optimal sphere. We found that, when  $n_{mon}$  is  $\sim 100$ , the results are not sensitive to the values of  $z_c$  and  $\alpha$ . The results below are for a simple cubic lattice,  $z_c = 6$  and  $\alpha = z_c(z_c - 2)/3$ .<sup>28</sup>

Shown in Figure 7 are the percolation transition and phase boundary calculated from the theory of Zilman and Safran for a CTAB+KBr solution. The percolation transition is near the point where  $g_{sph} \approx g_{jun}$ . The phase transition is predicted in the region where branched micellar aggregates are most stable.

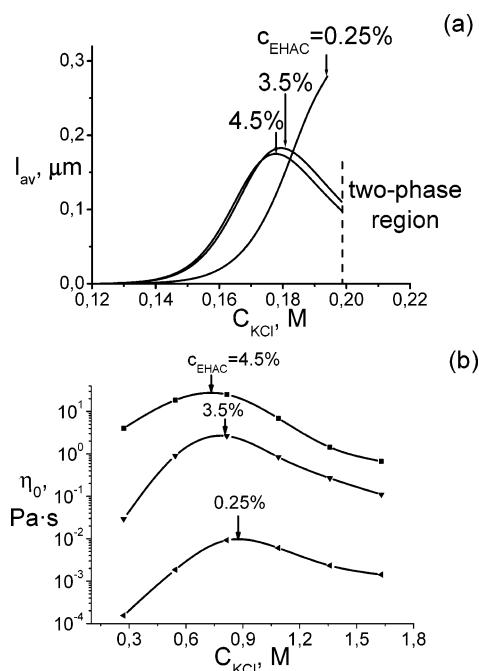
The formation of a network has a substantial effect on the viscosity of a solution. Although the Zilman and Safran theory does not allow direct calculation of the viscosity, useful information can be obtained by calculating the average micellar length  $l_{av}$ . Growth of wormlike micelles leads to an increase in the contour length between end-caps. Micellar branching tends to decrease the average micellar length. When a network forms, this decrease overwhelms the increase of  $l_{av}$  owing to micellar growth, and there is a maximum of  $l_{av}$ . On the other hand, the experimentally observable maximum of the zero-shear viscosity is frequently attributed to the formation of a micellar network.<sup>4,9–13</sup> Thus, predicting a maximum of the average micellar length, we can estimate the position of the expected maximum of the viscosity.

Figure 8 shows the experimental viscosity<sup>9</sup> for an EHAC+NaCl solution together with the calculated average micellar length. The model gives a maximum of the average length, and the location of that maximum is close to the location of the maximum on the viscosity–salinity curve. Phase separation is predicted upon an increase in salt concentration. A dense-network phase with a high concentration of junctions coexists with a sparse network. This is in qualitative agreement with the experiment,<sup>9</sup> where phase separation into viscous and nonviscous phases is observed at  $\sim 1.2$  M NaCl.

The results for EHAC+KCl solutions of varying surfactant concentrations are shown in Figure 9. Experiment shows that adding KCl<sup>10</sup> instead of NaCl<sup>9</sup> to an aqueous solution of EHAC shifts the viscosity peak to several times higher salinity. The Zilman–Safran theory combined with our model does not account for this effect and gives  $l_{av}$  maxima at substantially lower salinities than the maxima of the experimental<sup>10</sup> viscosity–salinity curves for the EHAC+KCl system. Nevertheless, the predicted effect of surfactant concentration on the position of the maximum is very similar to that exhibited by the experimental viscosity data. The maximum slightly shifts to lower salinity with the increase in surfactant concentration. Figure 9a also shows that, at low salt, prior to network-formation, longer micelles form at higher surfactant concentration. As we pass the percolation threshold corresponding to a maximum of  $l_{av}$  ( $3\phi_j = \phi_e$ ), the situation is reversed, and a more dense network (smaller  $l_{av}$ ) forms at higher surfactant concentration. Increasing salinity decreases surfactant concentration at percolation. All these predictions of the theory



**Figure 8.** The average length of micelles (solid line) calculated from the Zilman–Safran theory and experimental data (points) on the zero-shear viscosity<sup>9</sup> for an aqueous solution of EHAC+NaCl at 298 K.  $C_{EHAC} = 40$  mM. The percolation is at 180 mM of NaCl. The dashed line separates the two-phase and single-phase regions. The model parameters for EHAC are  $n_c = 22$  and  $a^{eff} = 0.70$  nm<sup>2</sup>.



**Figure 9.** (a) The average micellar length versus salinity calculated for an EHAC+KCl solution of varying surfactant concentration (indicated in wt %) at 313 K. (b) Experimental data on the viscosity at zero-shear rate for the same system.<sup>10</sup>

are reasonable. However, the maximum  $l_{av}$  values in Figure 9a decrease with surfactant concentration, whereas viscosity increases (see Figure 9b). This might be an erroneous prediction of the Zilman–Safran theory, although this might also be an indication of a denser network forming at a higher surfactant concentration and having a larger viscosity because of stronger intermicellar interactions. It would be an oversimplification to believe that there is a direct quantitative correlation between  $l_{av}$  values and viscosity in a network-forming system.  $l_{av}$  is an average of the structural characteristics of an equilibrium network and can only explain some trends in the change in viscosity. For salinities above 0.2 M KCl, the Zilman–Safran theory predicts phase separation that has not been observed experimentally.

Below, we compare calculated  $l_{av}$  with that found from rheological data,<sup>4</sup> even though these data give only a rough estimate of  $l_{av}$ .<sup>5</sup> Table 2 shows the average micellar length for CTAB+KBr as a function of surfactant concentration. In agreement with experiment,<sup>4</sup> the calculated length is almost independent of surfactant concentration in the given concentration range, although there is a trend toward decreasing  $l_{av}$  upon increasing surfactant concentration in both theory and experiment.

**Table 2. Calculated Maximum Average Micellar Length and Experimental Data<sup>4</sup> at the Onset of the Network for Aqueous Solutions of CTAB+KBr at 308 K**

| $C_{\text{CTAB}}, \text{M}$ | $l_{\text{av}}^{\text{exp}}, \mu\text{m}^4$<br>$C_{\text{KBr}} = 1.5 \text{M}$ | $l_{\text{av}}^{\text{calc}}, \mu\text{m}^a$ |
|-----------------------------|--|--|
| 0.1                         | 0.8  | 0.15 (0.24 M)                                |
| 0.2                         | 0.63   | 0.14 (0.23 M)                                |
| 0.3                         | 0.59   | 0.14 (0.22 M)                                |
| 0.35                        | 0.67   | 0.13 (0.22 M)                                |
| 0.4                         | 0.58   | 0.13 (0.22 M)                                |

<sup>a</sup> Shown in parentheses are salinities corresponding to calculated maxima of  $l_{\text{av}}$ .

Overall, the theory gives the correct order of the average micelle length while tending to underestimate its value significantly.

The Zilman–Safran theory gives the intensity of scattered light at zero wave vector and the correlation length, which both increase with salt concentration. Experimental data are available for  $\text{C}_{16}\text{PyClO}_3 + \text{NaClO}_3$ <sup>3</sup> and CTAB+KBr<sup>5</sup> solutions. However, a comparison of the calculated results with experiment is not informative because the Zilman–Safran theory predicts phase separation that is not observed in the range of salt concentration studied in experiment.<sup>3,5</sup>

## 7. Conclusion

A molecular-thermodynamic model is proposed for the aggregation free energy of branching portions of wormlike ionic micelles in 1:1 salt solution. An analytical solution is obtained for the linearized PB equation that is applicable to particles with saddle-like surface elements and reduces to the solutions known previously for planar, cylindrical, and spherical aggregates. This solution is not limited to micellar systems but may be applied to a broader range of systems that contain charged particles of complex shape. The new analytical solution is in excellent agreement with numerical results over the range of salinities, aggregate charge densities, and curvature radii typical of ionic surfactant systems with branching micelles.

Our model provides an extension of the previously known molecular-thermodynamic models<sup>34,36</sup> to aggregates of more complex shape. Our model predicts the sequence of stable aggregate morphologies, including a narrow bicontinuous zone intermediate between branched wormlike micelles and planar bilayers. The model reflects the effect of the molecular structure of the surfactant on the transitions between aggregates of different shapes. An increase in the length of the surfactant's tail leads to a decrease in the salt concentrations where shape transitions are predicted. Increasing the cross-sectional area of polar heads results in stronger steric repulsion and diminishes the stability of surfaces of lower curvature. Hence, the transition points shift to a higher salinity. These predictions agree with experiment for primary,<sup>54</sup> ternary,<sup>54</sup> and quaternary<sup>55–58</sup> ammonium salts. However, the experimental shift of the sphere-to-rod transition point is substantially greater than that predicted for this series of surfactants.

For predicting the properties of a spatial network of wormlike micelles, our aggregation free energy is used in the Zilman–Safran theory. The predictions are quite reasonable, although mostly not quantitative. This is because of the shortcomings of both the Zilman–Safran theory and of our model. The Zilman and Safran theory predicts the phase separation of a micellar solution at much lower salinity than in experiment.<sup>9</sup> Tuning the parameters of this theory does not lead to a satisfactory fit of the calculated and experimental saturation lines. Nevertheless, the theory of Zilman and Safran, up to now, remains the most powerful among the theoretical approaches for equilibrium micellar

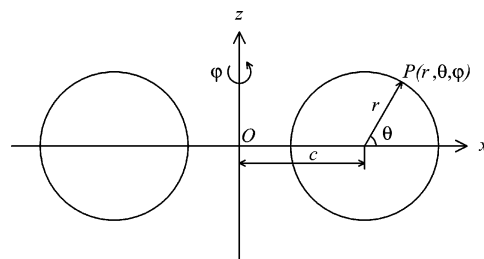


**Figure 10.** The coordinate  $(r, \theta, \varphi)$  system locates an arbitrary point  $P$  on the surface torus. Two circles of radius  $r$  are cross-sections of the torus of radii  $c$  and  $r$  by the  $POz$  plane. The orientation of the  $POz$  plane is given by angle  $\varphi$  between this plane and the  $xOz$  plane. The location of point  $P$  on the circle is specified by angle  $\theta$ .

networks. For further improvement of this theory, it is necessary to reflect more details of intermicellar interactions (other than the excluded-volume effect) and give a more adequate description of micellar stiffness than that in the existing version of the theory.

The major limitation of our model is that it does not reflect the specific ion effects.<sup>60,61</sup> The perspectives of refining our model are similar to those for molecular-thermodynamic models of aggregates of other shapes.<sup>34–38</sup> Perhaps the key issues of improving model performance are the specific ion effects, hydration of surfactant heads, and more adequate packing statistics for surfactant tails.<sup>36</sup> Nevertheless, our analytical model in its present form can be helpful for performing semiquantitative predictions and comparative studies of surfactants with a common counterion. This model can be extended in a straightforward manner to multivalent electrolytes.

**Acknowledgment.** The authors are grateful to Eric Reiner for sharing his knowledge about the relation between thermodynamics and electrostatics; to Natalia Smirnova and Andrey Vlasov for stimulating discussions; and to the Russian Foundation for Basic Research (Project #05-03-33267), the Federal Government (Grants #A04-2.11-418 and NSH-5557.2006.3), CRDF (Project#RCO1237), and the Schlumberger Research Center, Cambridge, for financial support.

## Appendix A: Approximate Analytical Solution of the Linearized PB Equation for the Torus

We use the orthogonal coordinate system  $(r, \theta, \varphi)$ <sup>62</sup> shown in Figure 10. The Cartesian coordinates of an arbitrary point  $P(r, \theta, \varphi)$  are expressed as

$$\begin{aligned} x(r, \theta, \varphi) &= (c + r \cos \theta) \cos \varphi \\ y(r, \theta, \varphi) &= (c + r \cos \theta) \sin \varphi \\ z(r, \theta, \varphi) &= r \sin \theta \end{aligned} \quad (\text{A1})$$

where  $c$  is the major radius of the torus centered at the origin. The torus's surface is specified by a single parameter,  $r = b$ . The Laplacian operator is defined by<sup>47</sup>

$$\nabla^2 \Psi = \frac{1}{r(c + r \cos \theta)} \left[ \frac{\partial}{\partial r} \left( r(c + r \cos \theta) \frac{\partial \Psi}{\partial r} \right) + \frac{\partial}{\partial \theta} \left( \frac{c + r \cos \theta}{r} \frac{\partial \Psi}{\partial \theta} \right) + \frac{\partial}{\partial \varphi} \left( \frac{r}{c + r \cos \theta} \frac{\partial \Psi}{\partial \varphi} \right) \right] \quad (\text{A2})$$

Our goal is to obtain an approximate analytic electric potential for the inner part of the torus that models the saddle-like element

(60) Zemb, T.; Belloni, L.; Dubois, M.; Aroti, A.; Leontidis, E. *Curr. Opin. Colloid Interface Sci.* **2004**, 9, 74–80.

(61) Soderman, O. *Curr. Opin. Colloid Interface Sci.* **2004**, 9, 154–157.

(62) Fixman, M. *J. Chem. Phys.* **1982**, 76, 6346–6353.

of the micellar junction. This goal is achieved by reducing the initial three-dimensional PB equation to an approximate one-dimensional equation. For the torus, the electric potential is axially symmetrical,  $\partial\Psi/\partial\varphi = 0$ , and therefore we omit the  $\varphi$  dependence from Laplacian A2. Introducing an effective average angle,  $\theta = \theta^*$ , and neglecting the second term in the brackets of eq A2, we obtain

$$\nabla^2\Psi = \frac{\partial^2\Psi}{\partial r^2} + \frac{c + 2r \cos \theta^*}{r(c + r \cos \theta^*)} \frac{\partial\Psi}{\partial r} \quad (\text{A3})$$

In eq A3, the factor in front of  $\partial\Psi/\partial r$  is equal to the double mean curvature of the torus's surface at the point located at  $(r, \theta = \theta^*)$ . Similarly, in spherical, cylindrical, and Cartesian coordinates, the factors in front of  $\partial\Psi/\partial r$  in the Laplacian are equal to the double mean curvature of a sphere, a cylinder, and a plane:  $2/r$ ,  $1/r$  and 0, respectively.

To model the saddle-like open element of the junction that, unlike the torus, does not have a pole in the center, we modify Laplacian A3 by writing

$$\nabla^2\Psi = \frac{\partial^2\Psi}{\partial r^2} + \frac{m}{r} \frac{\partial\Psi}{\partial r} \quad (\text{A4})$$

where  $m = (c + 2b \cos \theta^*)/(c + b \cos \theta^*)$  is constant. Expression A4 makes the linearized PB equation exactly solvable and does not have discontinuity at  $r = -c/\cos \theta^*$ . Eq A4 is close to the initial Laplacian A3 in the neighborhood of the aggregate,  $r \approx b$ , where we expect a major contribution to the thermodynamic functions for thin double layers.<sup>63</sup> In the limiting cases of spherical and cylindrical geometry, we have  $c \rightarrow 0$  and  $c \rightarrow \infty$ . This gives  $m = 2$  and  $m = 1$ , respectively, and eq A4 becomes exact. Equation A4 is also exact for a plane, where  $m = 0$ .

Using the Laplacian from eq A4, we obtain the linearized PB equation in a generalized one-dimensional form for spherical, cylindrical, saddle-like, and planar geometries:

$$\nabla^2\Psi = \frac{\partial^2\Psi}{\partial r^2} + \frac{m}{r} \frac{\partial\Psi}{\partial r} = \kappa^2\Psi \quad (\text{A5})$$

where  $m$  is the geometry-specifying parameter. Equation A5 has been studied numerically by Fogolari et al.,<sup>44</sup> who treated  $m$  as an empirical parameter. The analytical solution of eq A5 is given below.

The boundary conditions are the requirement of a vanishing electric field far from the aggregate and the Gauss law at the aggregate surface ( $\vec{r} = \vec{r}_0$ ):

$$(\nabla\Psi \cdot \vec{n})_{\vec{r}=\infty} = \left(\frac{d\Psi}{dr}\right)_{r=\infty} = 0 \quad (\text{A6})$$

$$(\nabla\Psi \cdot \vec{n})_{\vec{r}=\vec{r}_0} = \left(\frac{d\Psi}{dr}\right)_{r=b} = -\frac{\sigma}{\epsilon\epsilon_0} \quad (\text{A7})$$

Here we used the expressions for the gradient of the electric potential and for the unit normal to the torus surface in coordinate system A1:  $\nabla\Psi = (\partial\Psi/\partial r)\vec{i}_r + (1/r)(\partial\Psi/\partial\theta)\vec{i}_\theta + 1/(c + r \cos \theta)(\partial\Psi/\partial\varphi)\vec{i}_\varphi$  and  $\vec{n} = \vec{i}_r$ . We introduce the reduced electric potential  $u = e\Psi/kT$  and the reduced distance  $x = \kappa r$ . From eqs A5, A6, and A7, we have

$$\frac{d^2u}{dx^2} + \frac{m}{x} \frac{du}{dx} = u \quad (\text{A8})$$

$$\left.\frac{du}{dx}\right|_{x=\infty} = 0 \quad (\text{A9})$$

$$\left.\frac{du}{dx}\right|_{x=x_0} = -t \equiv -\frac{4\pi l_B}{e\kappa} \sigma \quad (\text{A10})$$

Using the substitution  $\omega(x) = x^p u(x)$ , where  $p = (m - 1)/2$ , eq A8 is rewritten as

$$x^2 \frac{d^2\omega}{dx^2} + x \frac{d\omega}{dx} - (x^2 + p^2)\omega = 0 \quad (\text{A11})$$

Equation A11 is the modified Bessel equation<sup>46</sup> with a general solution of  $\omega(x) = C_1 I_p(x) + C_2 K_p(x)$ , where  $I_p(x)$  and  $K_p(x)$  are the modified Bessel functions of order  $p$  of the first and second kind, respectively (see ref 47, p 709). Thus, the general solution of eq A8 is

$$u(x) = C_1 x^{-p} I_p(x) + C_2 x^{-p} K_p(x) \quad (\text{A12})$$

The boundary conditions A9 and A10 give  $C_1 = 0$  and  $C_2 = tx_0^p/[K_{p+1}(x_0)]$ , respectively, and hence the particular solution of eq A8 is

$$u(x) = t \left(\frac{x_0}{x}\right)^p \frac{K_p(x)}{K_{p+1}(x_0)} \quad (\text{A13})$$

where  $t$  is the reduced variable related to the charge density and ionic strength (see eq A10). Equation A13 describes the electrostatic potential for aggregates of different geometries, including aggregates with saddle-like surfaces that may be represented by the torus's elements. For a sphere,  $p = 1/2$ ; for a cylinder,  $p = 0$ ; and, for a plane,  $p = -1/2$ ; eq A13 reduces to previously known solutions.<sup>48</sup>

The analytic expression for the electrostatic free energy is derived by performing an isothermal charging process (Appendix C). Equations C2 and A13 together give

$$\frac{g_{el}}{kT} = \frac{1}{kT} \int_0^q \Psi(b) dq = \frac{a\kappa}{4\pi l_B} \int_0^t u(x_0) dt = \frac{a\kappa}{8\pi l_B} \frac{K_p(x_0)}{K_{p+1}(x_0)} t^2 \quad (\text{A14})$$

Here the electrostatic free energy,  $g_{el}$ , the aggregate charge,  $q$ , and the surface area,  $a$ , are calculated per surfactant molecule. As shown in Appendix C, the same value of  $g_{el}$  should also be obtained from eq A13 and the volume integration, eq B14 of Appendix B:

$$\frac{g_{el}}{kT} = \frac{a\kappa}{8\pi l_B} \frac{1}{x_0^m} \int_{x_0}^{\infty} \left[ \left(\frac{du}{dx}\right)^2 + u^2 \right] x^m dx \quad (\text{A15})$$

where we used the approximation  $d\vec{r} = r^m dr$  for the volume element.<sup>44,45</sup>

## Appendix B: Free Energy of the Electrical Double Layer at Equilibrium. A Variational Derivation

Calculation of the electrostatic free energy of electrical double layers has been widely discussed in the literature,<sup>49–51,64–67</sup>

(64) Marcus, R. A. *J. Chem. Phys.* **1955**, 23, 1057–1068.

(65) Trizac, E.; Hansen, J.-P. *J. Phys.: Condens. Matter* **1996**, 8, 9191–9199.

(66) Reiner, E. S.; Radke, C. J. *J. Chem. Soc., Faraday Trans.* **1990**, 86, 3901–3912.

(63) Ohshima, H.; Healy, T. W.; White, L. R. *J. Colloid Interface Sci.* **1982**, 90, 17–26.

including variational approaches,<sup>66,67</sup> different charging methods,<sup>49–51,64,65</sup> and force-integration technique.<sup>49</sup> The equivalence of different methods has been established,<sup>50,51</sup> but it has been stressed that care must be taken, for there are cases when different methods do not lead to identical results.<sup>65</sup>

In this work, we need two different formulas for calculating the electrostatic free energy: (1) the surface integral of the electrostatic potential is a most convenient route to obtain an analytical formula for the free energy; (2) the volume integral over the spatial distribution of the electric potential is more suitable for estimating the free energy from the numerical solution of the PB equation. In Appendices B and C, we derive both formulas and prove their equivalence for our system, summarizing some of the previously known results.<sup>49–51,68</sup>

Consider a charged aggregate of an arbitrary shape in a solution of 1:1 electrolyte. The charge of the aggregate is smeared over the aggregate surface with the charge density  $\sigma$ . The mobile ions around the aggregate neutralize the surface charge. The system is in contact with an infinitely large reservoir of given salinity. The dielectric permittivity of the surrounding solution and that of the aggregate interior are assumed to be uniform but may have different values in these parts of the system. Far from the aggregate, the electric field vanishes. The excess energy of the system over that of the bulk solution can be written as<sup>68,69</sup>

$$U = \frac{1}{2} \int_V [\sigma \delta(\vec{r} - \vec{r}_0) + e\rho_+(\vec{r}) - e\rho_-(\vec{r})] \Psi(\vec{r}) d\vec{r} \quad (\text{B1})$$

Here, the integration is over the volume of the system and includes the aggregate interior, its surface, and the electrical double layer that extends into the surrounding solution;  $\delta$  is the Dirac delta function,  $\vec{r}_0$  denotes the location of the surface,  $\Psi$  is the electric potential created by all the charges in the system (bulk and surface) and is set equal to zero far from the surface;  $\rho_+$  and  $\rho_-$  are the number densities of positive and negative ions in the system. The first integrand in eq B1 describes interactions of the surface charge with the electric field; the last two terms describe interactions of mobile ions with the electric field. The factor 1/2 is introduced to avoid double counting of interactions.

The electrostatic potential must satisfy the Poisson equation

$$\epsilon \epsilon_0 \nabla^2 \Psi(\vec{r}) = -[\sigma \delta(\vec{r} - \vec{r}_0) + e\rho_+(\vec{r}) - e\rho_-(\vec{r})] \quad (\text{B2})$$

where  $\epsilon_0$  is the dielectric permittivity of free space, and  $\epsilon$  is the dielectric permittivity of the medium.

Inserting eq B2 into eq B1 and applying Green's theorem,<sup>47</sup> we obtain

$$U = \frac{\epsilon \epsilon_0}{2} \int_V (\nabla \Psi)^2 dV - \frac{\epsilon \epsilon_0}{2} \int_{S_{\text{ext}}} \Psi \nabla \Psi \cdot \vec{n} dS \quad (\text{B3})$$

where the surface integral is over the external boundary of the system. This integral vanishes because  $\nabla \Psi \cdot \vec{n} = 0$  on that surface:

$$U = \frac{\epsilon \epsilon_0}{2} \int_V (\nabla \Psi)^2 dV \quad (\text{B4})$$

We assume that there is no electric field inside the aggregate,  $\nabla \Psi = 0$ , and therefore the integration in eq B4 is over the electrical double layer only.

Within the PB theory, the entropy of mobile ions in the double layer is that of an inhomogeneous ideal gas.<sup>70</sup> For the excess entropy of the system over that of the bulk solution, we write<sup>69</sup>

$$S = -k \sum_{i=\pm} \int_V [\rho_i (\ln \rho_i \Lambda_i^3 - 1) - \rho_i^0 (\ln \rho_i^0 \Lambda_i^3 - 1)] d\vec{r} \quad (\text{B5})$$

where  $\Lambda_i$  is the de Broglie thermal wavelength of ions  $i$ , and  $\rho_i^0$  is the density of ions  $i$  in the bulk solution. The first integrand in eq B5 is the contribution of ions  $i$  to the entropy density at point  $\vec{r}$ ; the second integrand is the same quantity in the bulk solution. Because we are estimating the electrostatic part of total thermodynamic functions, we drop the immaterial reference parts of the thermodynamic quantities, assuming that the internal degrees of freedom of the ions do not depend on their location in the system. For example, we write  $\mu_i = kT \ln \rho_i^0 \Lambda_i^3$  for the chemical potential of ions in the bulk.

The excess grand potential of the system over that of the bulk solution is<sup>69,70</sup>

$$\Omega[\rho_+, \rho_-, \Psi] = U - TS - \sum_{i=\pm} \int_V \mu_i (\rho_i(\vec{r}) - \rho_i^0) d\vec{r} \quad (\text{B6})$$

where  $\mu_i$  is the electrochemical potential of species  $i$ . The grand potential  $\Omega$  is a functional of profiles  $\rho_+(\vec{r})$ ,  $\rho_-(\vec{r})$ , and  $\Psi(\vec{r})$ . Equilibrium profiles correspond to a minimum of the grand potential and are obtained by the functional minimization of  $\Omega$ .<sup>68–71</sup> These profiles are not independent, but are related by the Poisson equation of electrostatics, eq B2. We substitute the solution of the Poisson equation for the electrical potential,<sup>47</sup>  $\Psi(\vec{r}) = [1/(4\pi\epsilon\epsilon_0)] \int_V [(\sigma \delta(\vec{r}' - \vec{r}_0) + e\rho_+ - e\rho_-)/(|\vec{r} - \vec{r}'|)] d\vec{r}'$ , into eq B1. Combining eqs B1, B5, and B6, and evaluating functional derivatives of  $\Omega$  with respect to  $\rho_i(\vec{r})$ , we obtain

$$\frac{\delta \Omega}{\delta \rho_i} = z_i e \Psi + kT \ln \rho_i \Lambda_i^3 - \mu_i = 0 \quad (\text{B7})$$

where  $z_i$  denotes “+” and “−” for positively and negatively charged ions, respectively. The equilibrium condition, eq B7, leads immediately to the Boltzmann distribution of ions

$$\rho_i(\vec{r}) = \rho_i^0 \exp(-z_i e \Psi(\vec{r})/kT) \quad (\text{B8})$$

and hence to the PB equation

$$\nabla^2 \Psi(\vec{r}) = -\frac{1}{\epsilon \epsilon_0} [\sigma \delta(\vec{r} - \vec{r}_0) + \sum_{z_i=\pm} z_i e \rho_i^0 \exp(-z_i e \Psi(\vec{r})/kT)] \quad (\text{B9})$$

The solution of eq B9 gives the electric potential  $\Psi(\vec{r})$  in the double layer. The spatial distribution of ions  $\rho_i(\vec{r})$  is calculated from eq B8. Combining eqs B4, B5, B6, and B7, we obtain the excess grand potential of the system in equilibrium:

$$\Omega = \frac{\epsilon \epsilon_0}{2} \int_V (\nabla \Psi)^2 d\vec{r} + kT \int_V \sum_{z_i=\pm} \left[ \rho_i \left( \ln \frac{\rho_i}{\rho_i^0} - 1 \right) + \rho_i^0 \right] d\vec{r} \quad (\text{B10})$$

The same equation for the excess grand potential is obtained using a charging process, eq C2, as shown in Appendix C.

(67) Sharp, K. A.; Honig, B. *J. Phys. Chem.* **1990**, *94*, 7684–7692.

(68) Trizac, E.; Hansen, J.-P. *Phys. Rev. E* **1997**, *56*, 3137.

(69) Borukhov, I.; Andelman, D.; Orland, H. *Macromolecules* **1998**, *31*, 1665–1671.

(70) Barrat, J.-L.; Hansen, J.-P. *Basic Concepts for Simple and Complex Liquids*; University Press: Cambridge, 2003.

(71) Zhulina, E. B.; Borisov, O. V. *J. Chem. Phys.* **1997**, *107*, 5952–5967.



A similar derivation gives the electrostatic free energy that corresponds to the linearized PB equation. For a weakly inhomogeneous system, the first integrand of eq B5 can be expanded to second order in the local densities  $\rho_i$  around their values in the bulk solution  $\rho_i^0$ :<sup>68</sup>

$$S = -k \int_V \sum_{z_i=\pm} \left[ (\rho_i - \rho_i^0) \ln \rho_i^0 \Lambda_i^3 + \frac{1}{2\rho_i^0} (\rho_i - \rho_i^0)^2 \right] d\vec{r} \quad (\text{B11})$$

Using eq B11 in eq B6, the functional minimization of the grand potential leads to the linearized form of the Boltzmann distribution and the linearized PB equation:

$$\rho_i = \rho_i^0 \left( 1 - \frac{z_i e \Psi}{kT} \right) \quad (\text{B12})$$

$$\nabla^2 \Psi(\vec{r}) = -\frac{\sigma \delta(\vec{r} - \vec{r}_0)}{\epsilon \epsilon_0} + \kappa^2 \Psi(\vec{r}) \quad (\text{B13})$$

where  $\kappa = (4\pi l_B \sum_{z_i=\pm} \rho_i^0)^{1/2}$  is the inverse Debye length. The equilibrium excess grand potential in the case of weak inhomogeneity is

$$\Omega = \frac{\epsilon \epsilon_0}{2} \int_V (\nabla \Psi)^2 d\vec{r} + \frac{\kappa^2 \epsilon \epsilon_0}{2} \int_V \Psi^2 d\vec{r} \quad (\text{B14})$$

Equation B14 can also be obtained using a charging process, eq C2, as shown in Appendix C.

### Appendix C: Calculation of the Electrostatic Free Energy by a Charging Process

Equations B10 and B14 for the electrostatic free energy involve volume integrations and are not convenient for deriving analytical expressions. A simpler alternative is provided by applying a charging process.<sup>49–51,64,65</sup> Because we compare the results of both methods, it is instructive to show that these two methods are quantitatively equivalent<sup>49–51,64,65</sup> for our system.

Consider a charged aggregate in solution, the same system described in Appendix B. The temperature and the chemical potentials of all species are specified because the system is in equilibrium with the large external reservoir of solution. The system volume is given by the definition of its boundaries. The only remaining variable that determines the equilibrium state of our system is the surface charge,  $Q$ .<sup>49,51</sup> The differential of the free energy is expressed as<sup>49,51</sup>

$$d\Omega = \Psi dQ$$

where  $\Psi$  is the potential on the aggregate surface. In a more general case of a nonuniform distribution of the electric potential over the surface, we have

$$d\Omega = \int_S \Psi d\sigma dS \quad (\text{C1})$$

Integration of eq C1 over the charge density gives the electrostatic contribution to the free energy:

$$\Omega = \int_S dS \int_0^\sigma \Psi d\sigma \quad (\text{C2})$$

Equation C2 is equivalent to the free energy expressions of Appendix B, as shown below using the method of ref 51.

The surface charge density and the electric field near the surface are related by the Gauss law:<sup>72</sup>

$$\{\epsilon \nabla \Psi\}_2 \cdot \vec{n} - \{\epsilon \nabla \Psi\}_1 \cdot \vec{n} = -\sigma / \epsilon_0 \quad (\text{C3})$$

where  $\vec{n}$  is the outward unit normal to the surface, the dot stands for the scalar product of the vectors, and indexes 2 and 1 denote the outer and inner sides of the surface, respectively. Substituting eq C3 into eq C1, we obtain

$$d\Omega = \epsilon_0 \int_S \{\Psi d[\epsilon \nabla \Psi]\}_1 \cdot \vec{n} dS - \epsilon_0 \int_S \{\Psi d[\epsilon \nabla \Psi]\}_2 \cdot \vec{n} dS \quad (\text{C4})$$

We integrate the identity

$$\nabla \cdot (\Psi d[\epsilon \nabla \Psi]) = \nabla \Psi \cdot d[\epsilon \nabla \Psi] + \Psi (\nabla \cdot d[\epsilon \nabla \Psi]) = \frac{1}{2} d[\epsilon (\nabla \Psi)^2] + \Psi d[\nabla \cdot (\epsilon \nabla \Psi)] \quad (\text{C5})$$

over the volume of the system but exclude the charged surface where  $\Psi d[\epsilon \nabla \Psi]$  is singular. The notation  $\nabla \cdot \vec{l}$  stands for the divergence of vector  $\vec{l}$ . Applying the Gauss theorem<sup>47</sup> to the left-hand side of eq C5, we obtain

$$\int_S \{\Psi d[\epsilon \nabla \Psi]\}_1 \cdot \vec{n} dS - \int_S \{\Psi d[\epsilon \nabla \Psi]\}_2 \cdot \vec{n} dS = \frac{1}{2} \int_V d[\epsilon (\nabla \Psi)^2] d\vec{r} + \int_V \Psi d[\nabla \cdot (\epsilon \nabla \Psi)] d\vec{r} \quad (\text{C6})$$

In eq C6, the surface integrals are over the inner (1) and over the outer (2) sides of the charged surface ( $S$ ) and emerge as a result of excluding this surface from the integration region.<sup>72</sup> The dielectric permittivity in the volume integrals of eq C6 changes stepwise and has constant values of  $\epsilon_1$  and  $\epsilon_2$  for integration inside and outside the aggregate, respectively. The surface integral over the external boundary of the system vanishes because  $\nabla \Psi \cdot \vec{n} = 0$  on that boundary. Comparing eq C4 and eq C6, we write

$$d\Omega = \frac{\epsilon_0}{2} \int_V d[\epsilon (\nabla \Psi)^2] d\vec{r} + \epsilon_0 \int_V \Psi d[\nabla \cdot (\epsilon \nabla \Psi)] d\vec{r} \quad (\text{C7})$$

Integrating the differentials in front of the square brackets in eq C7 and carrying out the second integral of eq C7 by parts yields

$$\Omega = \frac{\epsilon_0}{2} \int_V \epsilon (\nabla \Psi)^2 d\vec{r} + \epsilon_0 \int_V \Psi \nabla \cdot (\epsilon \nabla \Psi) d\vec{r} - \epsilon_0 \int_0^\Psi \int_V \nabla \cdot (\epsilon \nabla \Psi) d\Psi d\vec{r} \quad (\text{C8})$$

Assuming that, inside the aggregate, the electric charge  $\epsilon_0 \nabla \cdot (\epsilon \nabla \Psi)$  and the electric field  $\nabla \Psi$  are absent, the region of integration in eq C8 is reduced to the double layer; the aggregate surface is not included. In the double layer, the permittivity is assumed to be uniform:  $\epsilon = \epsilon_2$ . Expressing the last two terms of eq C8 with the aid of the Poisson equation, eq B2, we obtain

$$\Omega = \frac{\epsilon_0}{2} \int_V (\nabla \Psi)^2 d\vec{r} - \int_V [\epsilon \rho_+ - \epsilon \rho_-] \Psi d\vec{r} + \int_0^\Psi \int_V [\epsilon \rho_+ - \epsilon \rho_-] d\Psi d\vec{r} \quad (\text{C9})$$

where volume integration is performed over the aggregate exterior.

(72) Tamm, I. E. *Fundamentals of the Theory of Electricity*; Mir Publishers: Moscow, 1979.

Substitution of the Boltzmann distribution, eq B8, into eq C9 and integration of the last term over  $\Psi$  gives eq B10. Substituting the linearized Boltzmann distribution, eq B12, into eq C9, we obtain eq B14.

### Nomenclature

$A$  — surface area  
 $a$  — surface area per surfactant molecule  
 $a_0$  — surface area shielded by surfactant's headgroup  
 $a^{\text{eff}}$  — effective cross-section of surfactant's headgroup  
 $B$  — geometry-dependent parameter defined after eq 8  
 $b$  — minor radius of torus  
 $C_{\text{salt}}$  — concentration of added salt  
 $c$  — major radius of torus  
 $e$  — elementary positive charge  
 $f$  — free energy of micellar network per lattice site  
 $g$  — aggregation free energy per surfactant molecule  
 $K_\nu(x)$  — modified Bessel function of the second kind of order  $\nu$   
 $k$  — Boltzmann's constant  
 $L$  — Kuhn segment length  
 $l_s$  — length of surfactant's hydrocarbon tail  
 $l_B$  — Bjerrum length  
 $l_{\text{av}}$  — average segment of micellar network  
 $m$  — geometry-dependent parameter defined by eq 11  
 $N$  — number of Kuhn segments in the chain  
 $N_A$  — Avogadro's number  
 $n_C$  — number of carbon atoms in the hydrocarbon tail of surfactant  
 $\vec{n}$  — outward unit normal to the surface  
 $n_{\text{mon}}$  — aggregation number of "minimal" micelle  
 $n_{\text{tor}}$  — aggregation number of toroidal part of the junction  
 $p$  — geometry-dependent parameter defined by eq 11  
 $q$  — electric charge per surfactant molecule  
 $r_i$  — radius of aggregate of geometry  $i$   
 $r$  — radial coordinate, see Figure 10  
 $T$  — temperature  
 $t$  — reduced charge density defined by eq 10  
 $u$  — reduced electric potential  
 $u_0$  — reduced electric potential on micellar surface  
 $V$  — volume  
 $v_s$  — volume of surfactant's hydrocarbon tail

$x$  — reduced radial coordinate  
 $x_0$  — reduced coordinate of aggregate surface  
 $z_c$  — coordination number of the lattice

### Greek Symbols

$\alpha$  — lattice parameter  
 $\gamma$  — interfacial tension  
 $\delta$  — relative deviations between the numerical and analytical values  
 $\epsilon$  — dielectric permittivity of the medium  
 $\epsilon_0$  — dielectric permittivity of free space  
 $\eta$  — volume fraction  
 $\theta$  — angular coordinate, see Figure 1  
 $\kappa$  — inverse Debye length  
 $\sigma$  — surface charge density  
 $\phi_j$  — volume fraction of junctions  
 $\phi_e$  — volume fraction of end-caps  
 $\phi$  — total volume fraction of surfactant  
 $\varphi$  — angular coordinate, see Figure 1  
 $\Psi$  — electric potential  
 $\Omega$  — grand thermodynamic potential

### Superscripts

\* — optimal value  
 I, II — approximations for free energy explained prior to eq 15  
 num — numerical  
 anal — analytical

### Subscripts

cell — micellar cell  
 cyl — cylindrical geometry  
 def — deformation contribution  
 el — electrostatic contribution  
 int — interfacial contribution  
 jun — junction geometry  
 pl — planar geometry  
 sph — spherical geometry  
 st — steric contribution  
 tor — toroidal geometry

LA061087Q